

HDHumans: A Hybrid Approach for High-fidelity Digital Humans

MARC HABERMANN, Max Planck Institute for Informatics

LINGJIE LIU, Max Planck Institute for Informatics

WEIPENG XU, Meta Reality Labs

GERARD PONS-MOLL, University of Tuebingen

MICHAEL ZOLLHOEFER, Meta Reality Labs

CHRISTIAN THEOBALT, Max Planck Institute for Informatics

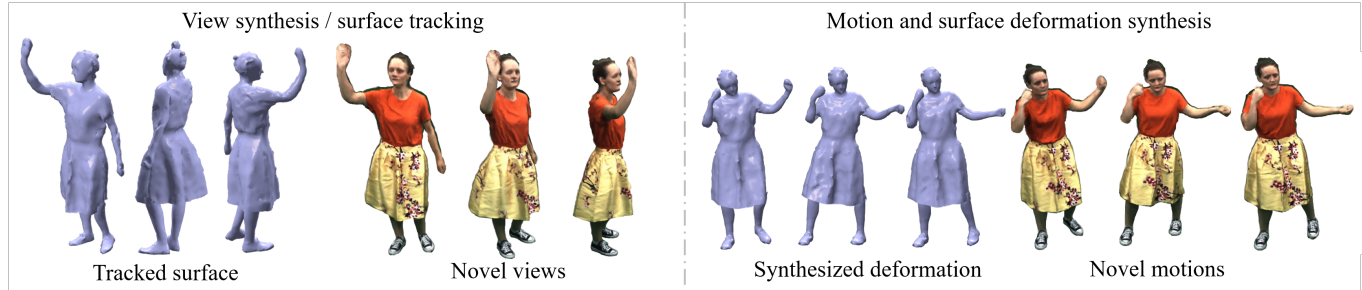


Fig. 1. We propose a method for photo-realistic human synthesis given an arbitrary camera pose and a potentially unseen skeletal motion. Our method is also able to handle loose types of clothing such as skirts, since we jointly learn the dense and space-time coherent deforming geometry of the human surface (including the dynamic clothing) along with a neural radiance field.

Photo-real digital human avatars are of enormous importance in graphics, as they enable immersive communication over the globe, improve gaming and entertainment experiences, and can be particularly beneficial for AR and VR settings. However, current avatar generation approaches either fall short in high-fidelity novel view synthesis, generalization to novel motions, reproduction of loose clothing, or they cannot render characters at the high resolution offered by modern displays. To this end, we propose HDHumans, which is the first method for HD human character synthesis that jointly produces an accurate and temporally coherent 3D deforming surface and highly photo-realistic images of arbitrary novel views and of motions not seen at training time. At the technical core, our method tightly integrates a classical deforming character template with neural radiance fields (NeRF). Our method is carefully designed to achieve a synergy between classical surface deformation and NeRF. First, the template guides the NeRF, which allows synthesizing novel views of a highly dynamic and articulated character and even enables the synthesis of novel motions. Second, we also leverage the dense pointclouds resulting from NeRF to further improve the deforming surface via 3D-to-3D supervision. We outperform the state of the art quantitatively and qualitatively in terms of synthesis quality and resolution, as well as the quality of 3D surface reconstruction.

CCS Concepts: • **Computing methodologies** → **Motion capture**; *Motion capture*; *Mesh geometry models*.

Additional Key Words and Phrases: human synthesis, neural synthesis, human modeling, human performance capture

Authors' addresses: Marc Habermann, Max Planck Institute for Informatics, mhaberma@mpi-inf.mpg.de; Lingjie Liu, Max Planck Institute for Informatics, liu@mpi-inf.mpg.de; Weipeng Xu, Meta Reality Labs, wxu@fb.com; Gerard Pons-Moll, University of Tuebingen, gerard.pons-moll@uni-tuebingen.de; Michael Zollhofer, Meta Reality Labs, zollhofer@fb.com; Christian Theobalt, Max Planck Institute for Informatics, theobalt@mpi-inf.mpg.de.

1 INTRODUCTION

Photo-realistic synthesis of digital humans is a very important research topic in graphics and computer vision. Specially, with the recent developments of VR and AR headsets, it has become even more important, since photo-real human avatars can be used to populate virtual or augmented real scenes. The classical approach to achieve this goal would be the manual creation of human avatars by means of 3D modeling including meshing, texturing, designing material properties, and many more manual steps. However, this process is not only tedious and time-consuming, but it also requires expert knowledge, preventing these techniques from being adopted by non-expert users. A promising alternative is to create such digital human avatars from video captures of real humans. The goal of our approach is to create controllable and highly photo-realistic characters at high resolution solely from multi-view video.

This idea was already subject of previous research works that can be broadly categorized based on the employed representation. Some approaches explicitly model the human's surface as a mesh and employ texture retrieval techniques [Casas et al. 2014; Xu et al. 2011] or deep learning [Habermann et al. 2021] to generate realistic appearance effects. However, the synthesis quality is still limited and the recovered surface deformations are of insufficient quality because they are driven purely by image-based supervision. Other works solely synthesize humans in image space [Chan et al. 2019; Liu et al. 2020b, 2019b]. These approaches however suffer from 3D inconsistency when changing viewpoint. Recently, first attempts have also been proposed to combine a neural radiance field with a naked human body model [Chen et al. 2021; Liu et al. 2021; Peng et al. 2021a,b; Xu et al. 2021]. These works have demonstrated that

a classical mesh-based surface can guide a neural radiance field (NeRF) [Mildenhall et al. 2020] for image synthesis. However, they only use a naked human body model or skeleton representation as a coarse proxy. Thus, they do not model the underlying deforming surface well, and in consequence they only work for subjects wearing tight clothing. In stark contrast, we for the first time demonstrate how a NeRF can be conditioned on a *densely deforming* template and we even show that improvements can be achieved in the other direction as well where the NeRF is guiding the mesh deformation.

In contrast to prior work, we propose a tightly coupled hybrid representation consisting of a classical deforming surface mesh and a neural radiance field defined in a thin shell around the surface. On the one hand, the surface mesh guides the learning of the neural radiance field, enables the method to handle large motions and loose clothing, and leads to a more efficient sampling strategy along the camera rays. On the other hand, the radiance field achieves a higher synthesis quality than pure surface-based approaches, produces explicit 3D constraints for better supervision of explicit surface deformation networks, and helps in overcoming local minima due to the local nature of color gradients in image space. This tight coupling between explicit surface deformation and neural radiance fields creates a two-way synergy between both representations. We are able to jointly capture the detailed underlying deforming surface of the clothed human and also employ this surface to drive a neural radiance field, which captures high-frequency detail and texture. More precisely, our method takes skeletal motion as input and predicts a motion-dependent deforming surface as well as a motion- and view-dependent neural radiance field that is parameterized in a thin shell around the surface. In this way, the deforming surface acts as an initializer for the sampling and the feature accumulation of the neural radiance field making it significantly (6 times) more efficient and, thus, enables training on 4K multi-view videos. The deforming surface mesh and the neural radiance field are tightly coupled during training such that the mesh drives the neural radiance field making it efficient and robust to dynamic changes. Furthermore, not only the neural radiance field is improved based on the tracked surface mesh, but it can also be used to refine the surface mesh, since the neural radiance field drives the mesh towards reconstructing finer-scale detail, such as cloth wrinkles, which are difficult to capture with image-based supervision alone. Thus, a two-way synergy between the employed classical and neural scene representation is created that leads to significantly improved fidelity. The results show that, compared to previous work, our approach not only reconstructs deforming surface geometry of higher quality, but also renders human images at much higher fidelity (see Figure 1). In summary, our technical contributions are:

- A novel approach for high-fidelity character synthesis that enables novel view and motion synthesis at a very high resolution, which cannot be achieved by previous work.
- A synergistic integration of a classical mesh-based and a neural scene representation for virtual humans that produces higher quality geometry, motion, and appearance than any of the two components in isolation.

To the best of our knowledge, this is the first approach that tightly couples a *deforming explicit mesh* and a neural radiance field, which

then enables photo-realistic rendering of neural humans *wearing loose clothing*. Our experiments demonstrate that we outperform the previous state of the art in terms of image synthesis quality and geometry reconstruction.

2 RELATED WORK

Mesh-based synthesis. Photo-realistic image synthesis of controllable characters is challenging due to the difficulty in capturing or predicting high-quality pose-dependent geometry deformation and appearance. Some works [Carranza et al. 2003; Collet et al. 2015; Hilsmann et al. 2020; Li et al. 2014; Zitnick et al. 2004] focus on free-viewpoint replay of the captured human performance sequence. Other works Casas et al. [2014]; Volino et al. [2014]; Xu et al. [2011] aim at the more challenging task of photo-realistic free-viewpoint synthesis for new body poses. Xu et al. [2011] approached this problem by first employing texture retrieval to find the nearest image based on the query body pose and viewpoint in a database and then applying texture stitching to synthesize a new texture map for the query pose and viewpoint. However, their method needs several seconds to generate a single frame. [Casas et al. 2014; Volino et al. 2014] accelerate the image synthesis process with a temporally coherent layered representation of appearance in texture space. These classical methods struggle with producing high-quality results due to the coarse geometric proxy, and have limited generalizability to new poses and viewpoints, which are very different from those in the database. To improve the synthesis quality and generalizability, Habermann et al. [2021] proposes a method for learning a 3D virtual character model with pose-dependent geometry deformations and pose- and view-dependent textures in a weakly supervised way from multi-view videos. While great improvements have been made, some fine-scale details are missing in the results, because of the difficulty in the optimization of deforming polygon meshes with only images as supervision. In this work, we observed that deforming implicit fields is more flexible (e.g., no need of using regularization terms to keep the mesh topology), thus leading to more stable and efficient training. However, the rendering of implicit fields is time-consuming, and editing implicit representations is much more difficult than editing explicit representations, e.g., meshes. Hence, our method unifies the implicit fields and explicit polygon meshes into a new representation joining the advantages from both worlds.

Image-based synthesis. Generative Adversary Networks (GANs) have achieved great progress in image synthesis in recent years. To close the gap between the rendering of a coarse geometric proxy and realistic renderings, many works formulate the mapping from the coarse rendering to a photo-realistic rendering as an image-to-image translation problem. These works take the renderings of a skeleton [Chan et al. 2019; Kappel et al. 2020; Li et al. 2019; Pumarola et al. 2018; Shysheya et al. 2019; Zhu et al. 2019], a dense mesh [Grigor'ev et al. 2019; Liu et al. 2020b, 2019b,a; Neverova et al. 2018; Prokudin et al. 2021; Raj et al. 2021; Sarkar et al. 2020; Wang et al. 2018], or a joint position heatmap [Aberman et al. 2019; Ma et al. 2017, 2018] as the input to image-to-image translation and output realistic renderings. While these methods can produce high-quality images from a single view, they are not able to synthesize view-consistent videos when changing camera viewpoints. This is mainly due to the

fact that the convolution kernel used is not 3D transformation equivariant and the skip connection in the employed image-to-image translation architectures propagate only 2D local information and bypasses 3D structure reasoning. Furthermore, since these methods heavily rely on the image-to-image translation network, the refinement simply applied in the 2D image space leads to missing limbs and image stitching artifacts in the outputs, especially when there is severe noise in the training data. In contrast, our method directly optimizes the geometry deformations and appearance in 3D space, so it is able to produce temporally- and view-consistent photo-realistic animations of characters.

Volume-based and hybrid approaches. Recently, some methods have demonstrated impressive results on novel view synthesis of static scenes by using neural implicit fields [Mildenhall et al. 2020; Niemeyer et al. 2020; Oechsle et al. 2021; Sitzmann et al. 2019; Wang et al. 2021; Yariv et al. 2021, 2020] or hybrid representations [DeVries et al. 2021; Hedman et al. 2021; Liu et al. 2020a; Reiser et al. 2021; Yu et al. 2021] as scene representations. Great efforts have been made to extend neural representations to dynamic scenes. Neural Volumes [Lombardi et al. 2019] and its follow-up work [Wang et al. 2020] use an encoder-decoder network to learn a mapping from reference images to 3D volumes for each frame of the scene, followed by a volume rendering technique to render the scene. Several works extend NeRF [Mildenhall et al. 2020] to dynamic scene modeling with a dedicated deformation network [Park et al. 2020, 2021; Pumarola et al. 2020; Treitschk et al. 2021], scene flow fields [Li et al. 2020], or space-time neural irradiance fields [Xian et al. 2020]. Many works focus on human character modeling. [Kwon et al. 2021; Peng et al. 2021b] assigns latent features on the vertices of the SMPL model and uses them as anchors to link different frames. Lombardi et al. [2021] introduce a mixture of volume primitives for the efficient rendering of human actors. These methods can only playback a dynamic scene from novel views but are not able to generate images for novel poses. To address this issue, several methods propose articulated implicit representations for human characters. A-NeRF [Su et al. 2021] proposes an articulated NeRF representation based on a human skeleton for human pose refinement. Gafni et al. [2021] conditions NeRF on the head poses and facial expressions for upper body synthesis. Recent works [Anonymous 2022; Chen et al. 2021; Jiakai et al. 2021; Liu et al. 2021; Noguchi et al. 2021; Peng et al. 2021a; Xu et al. 2021] present a deformable NeRF representation, which unwarps different poses to a shared canonical space with inverse kinematic transformations and residual deformations. Moreover, HumanNeRF Weng et al. [2022] has shown view-synthesis for human characters given only a monocular RGB video for training the radiance field. Most of these works cannot synthesize pose-dependent dynamic appearance, are not applicable to large-scale datasets that include severe pose variations, and have limited generalizability to new poses. The most related work to our proposed method is Neural Actor [Liu et al. 2021], which uses a texture map as a structure-aware local pose representation to infer dynamic deformation and appearance. In contrast to our method, they only use a naked human body model as a mesh proxy, and thus cannot model characters in loose clothes. Furthermore, they only employ the mesh proxy to guide the warping of NeRF but do not optimize the mesh. In consequence, this method cannot extract high-quality

surface geometry. Further, since the mesh proxy is not very close to the actual surface, it still needs to sample many points around the surface, which makes the training not fast enough to support for 4K resolution. Instead, we infer the dense deformation of a template that is assumed to be given, which is more efficient and enables the tracking of loose clothing. More importantly, our recovered NeRF even further refines the template deformations.

3 METHOD

The goal of our approach is to learn a unified representation of a dynamic human from multi-view video, which on the one hand allows to synthesize motion-dependent deforming geometry and on the other hand also enables photo-real synthesis of images displaying the human under novel viewpoints and novel motions. To this end, we propose an end-to-end approach, which solely takes a skeletal motion and a camera pose as input and outputs a posed and deformed mesh as well as the respective photo-real rendering of the human. Figure 2 shows an overview of the proposed method. At the core of our method is the synergistic combination of a person-specific deformable mesh with a neural radiance field. In the following, first, some fundamentals regarding neural radiance fields and the deformable human mesh model are provided, and their limitations are discussed (Section 3.1). Then, we introduce our mesh-guided neural radiance field, which allows synthesizing a dynamic performance of the actor from novel views and for unseen motions (Section 3.2). This proposed mesh guidance assumes a highly detailed, accurately tracked, and space-time coherent surface of the human actor. We however found that previous weakly-supervised performance capture approaches [Habermann et al. 2021, 2020] struggle with capturing high fidelity geometry, i.e. smaller clothing wrinkles. At the same time, volume-based surface representations [Mildenhall et al. 2020] seem to recover such geometric details when visualizing their view-dependent pointclouds, but they lack space-time coherence, which is essential for the proposed mesh guidance. To overcome this limitation, we leverage the geometric details to further refine the coarse (but space-time coherent) template deformations. In particular, we propose a NeRF-guided point cloud loss, which further improves the motion-dependent and deformable human mesh model (Section 3.3).

Data assumptions. Before we explain our method in detail, we give a brief description of the employed training data. For each actor, we employ C calibrated and synchronized cameras to collect a multi-view video of the person performing various types of motions. To segment the actor from the background, we apply color keying resulting in per-frame and view foreground masks. The skeletal motion of the actor that is input to our method is recovered using a commercial markerless motion capture software [TheCapture 2020]. Finally, we acquire a static textured mesh template of the person using a scanner [Treedys 2020] that is manually rigged to the skeleton. Note that our approach does not assume any 4D geometry in terms of per-frame scans or pointclouds as input.

Notation. The superscript $(\cdot)^r$ refers to a specific ray or pixel sampled from any of the camera views. The subscript $(\cdot)_i$ refers to the i th sample along the ray. Further, $(\cdot)_j$ denotes the j th vertex of the template mesh, and $(\cdot)_t$ refers to the t th frame of the video.

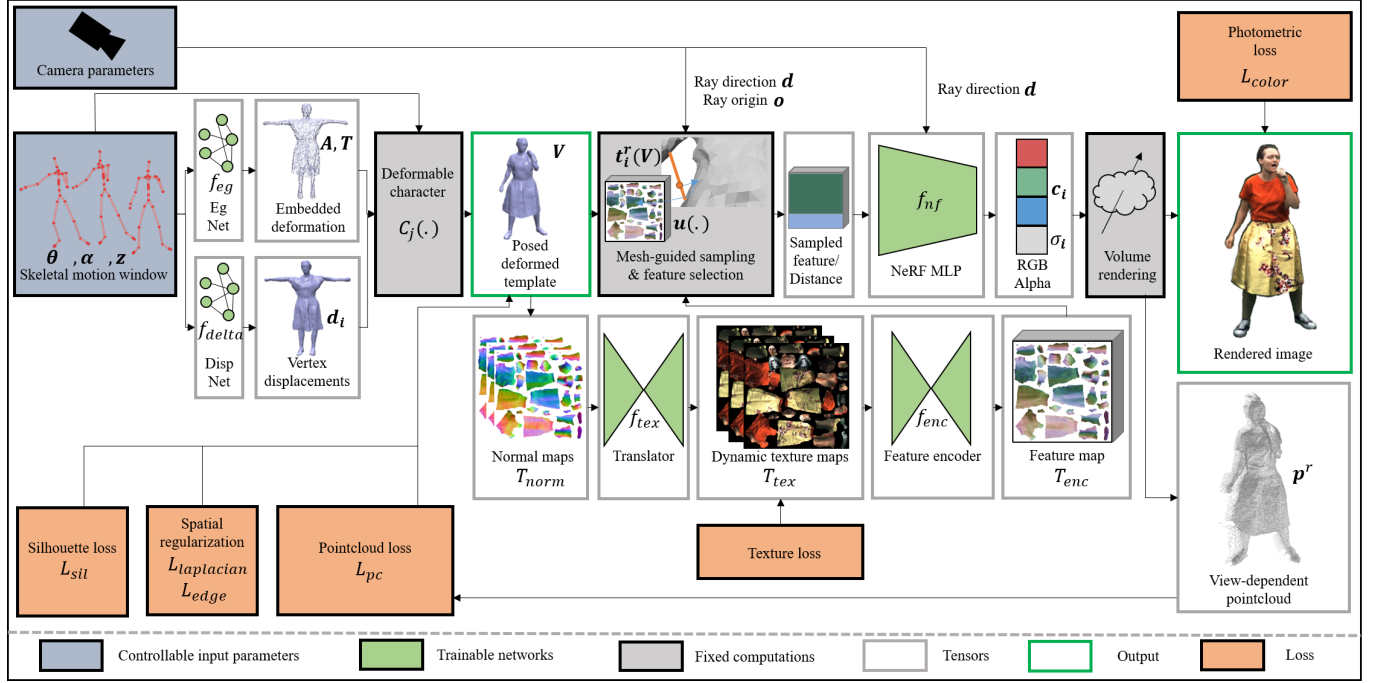


Fig. 2. Overview of the proposed approach. Our method takes as input a skeletal motion of the actor. Then, a motion-dependent and learned character representation poses and deforms the mesh template. From this mesh, we extract normal maps and translate them into dynamic texture maps, which are finally encoded in a feature map. When rendering a ray, samples along the ray are projected onto the character and the respective feature from the feature map is extracted. This is then used as a conditioning input to a NeRF, which renders the final image. From the NeRF, also view-dependent pointclouds can be extracted, which can then be used to again refine the deformation networks. This process can be iterated multiple times.

3.1 Human Mesh Model and Neural Radiance Fields

Before we dive into the proposed method, we discuss the fundamentals of the motion-dependent mesh deformation model, the concept of neural radiance fields, and their respective limitations.

3.1.1 Deformable Human Mesh Model. We aim at having a deformation model of the human body and clothing, which only depends on the skeletal motion $\mathcal{M} = \{(\theta_{t-T}, \alpha_{t-T}, z_{t-T}), \dots, (\theta_t, \alpha_t, z_t)\}$ and deforms the person-specific template such that motion-dependent clothing and body deformations can be modeled, e.g. the swinging of a skirt induced by the motion of the hips. Here, $\theta_t \in \mathbb{R}^{57}$, $\alpha_t \in \mathbb{R}^3$, and $z_t \in \mathbb{R}^3$ refer to the skeletal joint angles, the root rotation and translation, respectively. In practice, the time window is set to 3 ($T = 2$) and for the current character pose $(\theta_t, \alpha_t, z_t)$ we drop the frame subscript for readability in the following and assume the motion window is fixed. We leverage the character representation of Habermann et al. [2021]

$$C_j(\theta, \alpha, z, A, T, d_j) = v_j, \quad (1)$$

which takes the current skeletal pose, embedded deformation parameters $A, T \in \mathbb{R}^{K \times 3}$, where K denotes the number of graph nodes of an underlying graph, and the per vertex displacement $d_j \in \mathbb{R}^3$ for vertex j as input. It returns the posed and deformed vertex v_j .

In order to model the skeletal motion-dependent template deformation, embedded deformations [Sorkine and Alexa 2007; Sumner

et al. 2007] are learned by a motion-conditioned graph convolutional network

$$f_{eg, w_{eg}}(e(\mathcal{M})) = A, T \quad (2)$$

where $e(\cdot)$ is their proposed skeletal motion-to-graph encoding, and w_{eg} are the network weights. To capture dynamic details beyond the resolution of the embedded graph, a second graph convolutional network

$$f_{delta, w_{delta}}(d(\mathcal{M}))_j = d_j \quad (3)$$

learns the additional per-vertex displacements as a function of the skeletal motion. Here, $d(\cdot)$ is their proposed motion-to-vertex encoding and w_{delta} are the network weights. Now, inserting both networks into Equation 1 leads to the generative character model

$$C_j(\theta, \alpha, z, f_{eg, w_{eg}}(e(\mathcal{M})), f_{delta, w_{delta}}(d(\mathcal{M}))_j) = v_j \quad (4)$$

which is solely parameterized by the skeletal pose (θ, α, z) and the network outputs that are conditioned on the skeletal motion \mathcal{M} . The entire posed and deformed mesh can be derived by stacking the individual vertices into a matrix $V \in \mathbb{R}^{N \times 3}$ where N denotes the number of template vertices. Interestingly, the deformation networks can be trained purely from image data using a multi-view silhouette loss \mathcal{L}_{sil} and a dense rendering loss \mathcal{L}_{chroma} , as well as some spatial regularizers $\mathcal{L}_{spatial}$. We follow their proposed training procedure to obtain pre-trained deformation networks. For more details, we refer to [Habermann et al. 2021].

3.1.2 Neural Radiance Fields. A neural radiance field (NeRF) [Mildenhall et al. 2020] is a deep, volumetric scene representation of a static scene, which enables photo-realistic novel view synthesis. In detail, for rendering an image, each pixel is represented by a camera ray that has a normalized direction $d \in \mathbb{R}^3$ and an origin $o \in \mathbb{R}^3$. Then, $i \in \{0, \dots, K\}$ samples along the ray at positions

$$x_i = o + t_i d, \quad (5)$$

where $x_i \in \mathbb{R}^3$ and t_i is the depth along the ray, are drawn and fed into a Multi-layer Perceptron (MLP)

$$f_{\text{nf}, w_{\text{nf}}}(\gamma(x_i), \gamma(d)) = (c_i, \sigma_i) \quad (6)$$

which takes the positional encoding $\gamma(\cdot)$ of x_i and d as input. Then, the network predicts a color $c_i \in \mathbb{R}^3$ and a density value $\sigma_i \in \mathbb{R}$. Here, w_{nf} are the trainable network weights.

To obtain the final pixel color, the individual colors and densities are accumulated using volume rendering [Levoy 1990] according to

$$\tilde{c} = \sum_{i=0}^K T_i \alpha_i c_i \quad (7)$$

$$T_i = \prod_{j=0}^{i-1} (1 - \alpha_j) \quad (8)$$

$$\alpha_i = 1 - e^{-\delta_i \sigma_i} \quad (9)$$

where δ_i is the Euclidean distance between the sample points x_{i+1} and x_i .

3.1.3 Discussion. The main advantage of the proposed geometry-based character representation [Habermann et al. 2021] is that it can represent dynamically moving humans and that the reconstructed and synthesized geometry matches image silhouettes well and it shows some plausible coarse deformations. However, there is still a gap in terms of surface accuracy and the approach suffers from baked-in geometric details originating from the scanned template mesh, which remain almost rigid throughout the deformation. We suspect that this comes from the purely image-based supervision strategy, which prevents the template from being deformed more drastically with respect to the scan. While they enable the synthesis of loose clothing such as skirts, we also found that the learned dynamic texture and the final appearance in image space cannot reach the quality of volume-based neural rendering approaches for static scenes.

NeRF [Mildenhall et al. 2020] has shown state-of-the-art synthesis quality on *static* scenes. Interestingly, when training NeRF on humans, the recovered depth maps show detailed wrinkle patterns despite some noise and outliers. However, long compute time and the fact that the original NeRF formulation is limited to static scenes prevent it from being directly used on long dynamic scenes (around 20,000 frames), which we are targeting. Recently, human-specific follow-up works [Chen et al. 2021; Liu et al. 2021; Peng et al. 2021a,b; Xu et al. 2021] have been introduced. However, they usually rely on a naked human body model and do not account for non-rigid surface deformations, such as the dynamic movement of clothing. As a consequence, these works are limited to types of apparel that tightly align with the naked human body while loose clothes such as skirts are beyond their reach.

In the following, we address these problems of 1) limited geometric deformations caused by the purely image-based supervision, 2) limited synthesis quality of geometry-based representations, and 3) the limited types of apparel that can be synthesized by recent NeRF-based approaches. To this end, we propose a novel and non-trivial combination of a deformable mesh-based representation and a neural radiance field and show that one can overcome the above limitations by tightly coupling those two representations.

3.2 Mesh-guided Neural Radiance Fields

First, we want to establish a tight connection between the deforming human mesh model and a surrounding neural radiance field. Here, we assume the posed and deformed vertex positions V are given by our pre-trained character model (Equation 4). Next, we describe how the skeletal motion can be encoded in texture space, how such features can be attached to a neural radiance field, how to derive the final appearance, and how the mesh-guided NeRF can be supervised.

3.2.1 Motion-dependent Neural Texture. When thinking about defining motion-dependent features on the mesh surface, there usually is the problem of an one-to-many mapping [Bagautdinov et al. 2021; Liu et al. 2021], since (almost) similar motion can lead to various different images, i.e., wrinkle patterns on the clothing. This is due to the fact that the state of clothing does not only depend on the last few poses of the actor, but there exist also other factors. Examples are the initial state of clothing when the performance starts, external forces such as wind, and second order dynamics. On the one hand, reliably modeling all of these is intractable and on the other hand ignoring them leads to a blurred appearance [Habermann et al. 2021]. Similar to Liu et al. [Liu et al. 2021], we encode the actor’s pose $(\theta_t, \alpha_t, z_t)$ of frame t in the form of a normal map $\mathcal{T}_{\text{norm}, t} \in \mathbb{R}^{1024 \times 1024 \times 3}$, which is denoted by the function $m(\theta_t, \alpha_t, z_t) = \mathcal{T}_{\text{norm}, t}$. However, different to them we use the posed *and deformed* geometry for creating the normal maps. Thus, higher frequency geometric details are explicitly represented in the normal maps. Then a texture-to-texture translation network [Wang et al. 2018]

$$f_{\text{tex}, w_{\text{tex}}}(m(\theta_t, \alpha_t, z_t)) = f_{\text{tex}, w_{\text{tex}}}(\mathcal{T}_{\text{norm}, t}) = \mathcal{T}_{\text{tex}, t} \quad (10)$$

converts them into dynamic texture maps $\mathcal{T}_{\text{tex}, t} \in \mathbb{R}^{1024 \times 1024 \times 3}$, which contain realistic cloth wrinkle patterns. For creating the training pairs, the posed normal maps can be trivially computed from the posed and deformed mesh. For generating the ground truth texture maps $\mathcal{T}_{\text{tex}, \text{gt}, t} \in \mathbb{R}^{1024 \times 1024 \times 3}$, we leverage the multi-view texture stitching approach proposed by Alldieck et al. [Alldieck et al. 2018]. Simply using an ℓ_1 -loss for \mathcal{L}_{tex} between $\mathcal{T}_{\text{tex}, \text{gt}, t}$ and $\mathcal{T}_{\text{tex}, t}$ would still lead to blurry results for the above mentioned reasons. Thus, we employ a discriminator loss as proposed in the vid2vid architecture [Wang et al. 2018]. We found that this greatly reduces the problem of the one-to-many mapping.

Finally, we have a feature encoder based on the UNet architecture [Isola et al. 2017],

$$f_{\text{enc}, w_{\text{enc}}}(\mathcal{T}_{\text{tex}, t-T}, \dots, \mathcal{T}_{\text{tex}, t}) = \mathcal{T}_{\text{enc}, t} \quad (11)$$

which takes the generated textures $\mathcal{T}_{\text{tex}, t'}$ of the motion window $t' \in \{t-T, \dots, t\}$ by concatenating them along the last channel resulting in a texture tensor $\mathcal{T}_{\text{enc}, t} \in \mathbb{R}^{1024 \times 1024 \times 3(T+1)}$. The output of this

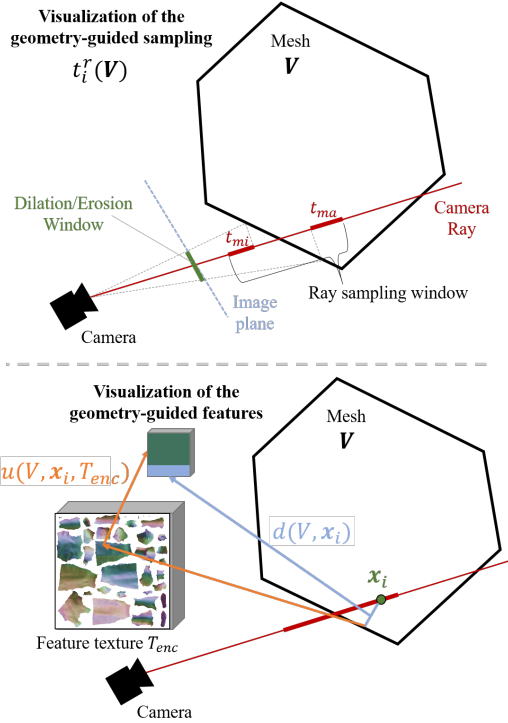


Fig. 3. Illustration of the geometry-guided neural radiance field sampling and feature assignment. Note that the mesh can efficiently guide the ray sampling and only samples close to the mesh have to be drawn (bold red line). Then, texture features and the signed distance to the surface can be used as a conditioning input to the NeRF MLP.

is a feature texture $\mathcal{T}_{enc,t} \in \mathbb{R}^{1024 \times 1024 \times 32}$ that will be later used as an input to the neural radiance field. Previous work [Liu et al. 2021] showed that encoding the texture into a feature space rather than directly using the generated texture as a conditioning input to NeRF improves the synthesis quality. Thus, we follow this design choice, however, we choose a UNet-based [Isola et al. 2017] encoder rather than a ResNet-based [He et al. 2016] architecture. This allows us to efficiently encode a higher resolution feature map (1024×1024 vs. 512×512 [Liu et al. 2021]). Further, since we predict appearance from motion rather than from a single pose [Liu et al. 2021], we also concatenate the per-pose textures $\mathcal{T}_{tex,t}$ in the feature channel.

3.2.2 Geometry-guided Sampling. Next, we describe how the NeRF sampling process can be represented as a function of the deforming mesh V given a ray r and therefore tightly connects the two representations. A visualization of this process is shown in Figure 3. Assuming the training camera and the ray r are fixed, the i th sample x_i along the ray is originally defined by Equation 5 where t_i is first sampled uniformly and later based on importance sampling. As r is fixed, o and d are pre-defined. However, we replace t_i with the following geometry-dependent function

$$t_i^r(V) = (1 + \frac{i}{S})(E(\Phi^r(V)) - t_{mi}) + \frac{i}{S}(D(\Phi^r(V)) + t_{ma}). \quad (12)$$

Here, $\Phi^r(V)$ is a depth renderer, which renders the depth map of the mesh with respect to the camera, and r indicates the specific

pixel that was rendered. The function $D(\cdot)$ represents the dilation operator, which computes the maximum depth value in the depth map around the sampled location r . Similarly, $E(\cdot)$ computes the eroded value or minimum value around the sampled location r . We choose a kernel size of 9×9 for both operators. The erosion and dilation ensure that the NeRF is also sampled on the foreground when the underlying mesh is erroneously not exactly overlaying the ground truth foreground mask. Moreover, t_{mi} defines the volume that is sampled in front of the actual surface, and similarly t_{ma} defines the volume that is sampled behind the actual surface by ensuring that the distance between the rendered depth and the depth of the sample point does not exceed t_{mi} and t_{ma} . We set $t_{mi} = t_{ma} = 4cm$ for all results. Lastly, S defines the number of samples along the ray. When sampling r , only pixels that project onto the eroded/dilated depth maps are considered. Otherwise, they are discarded during the NeRF evaluation described later.

This allows a more effective sampling of the neural radiance field since most samples are very close to the actual surface. In practice, we only need a single NeRF MLP in contrast to [Mildenhall et al. 2020], which employ a coarse and a fine MLP. Moreover, they draw 64 samples for the coarse MLP and 128 for the fine MLP. Since our mesh provides accurate sampling guidance, we only require 32 samples for generating photo-realistic results. This effectively means our mesh-guided sampling is 6 times more efficient than the baseline, which is especially important when training on 4K multi-view videos.

3.2.3 Geometry-guided Motion Features. The other important property, which is missing in the original NeRF approach, is that it can only render a *static* scene under novel views. However, we aim at synthesizing novel views and performances of *dynamic* scenes. Fortunately, the posed and deformed template can also help to enable the synthesis of dynamic scenes using our motion-dependent feature texture \mathcal{T}_{enc} . The main idea is that the motion-dependent deep features attached to the mesh can be propagated to the 3D ray samples (see Figure 3). Then, instead of evaluating the NeRF MLP on global coordinates, we condition the MLP on a surface relative encoding using the signed distance and the texture features. More specifically, Equation 6 is modified as

$$f_{inf,w_{nf}}(u(V, x_i, \mathcal{T}_{enc}), \gamma(d(V, x_i)), \gamma(d)) = (c_i, \sigma_i). \quad (13)$$

Here, $u(\cdot)$ takes the mesh V , the sample x_i along the ray, and the feature texture \mathcal{T}_{enc} as input and samples the feature texture at the UV coordinate of the closest point from x_i to the mesh resulting in a 32-dimensional feature. $d(\cdot)$ computes the signed and normalized distance between the mesh and the sample point. Here, points in the interior of the mesh have a negative sign, and the points outside the mesh have a positive sign. The term *normalized* means that the actual distance is divided either by t_{mi} or t_{ma} , depending on whether the sample point is inside or outside the mesh surface. A positional encoding [Mildenhall et al. 2020] is then applied to the distance value using 10 frequencies. Finally, the MLP also takes the positional encoding of the viewing direction using 4 frequencies.

Note that Equation 13 only depends on the skeletal motion \mathcal{M} (which then defines V and \mathcal{T}_{enc}) and the camera pose (which then defines x_i and d). Thus, this reformulation allows the network to

encode the dynamic motion of the actor and allows NeRF to handle dynamically moving humans. Since we represent the skeletal motion as a spatially varying texture map on the deforming geometry, the motion-dependent appearance effects can be encoded locally on the surface level, which improves the generalization compared to a global motion encoding.

3.2.4 Supervision. During training, we fix the pre-trained deformation networks f_{eg} and f_{delta} and the texture translation network f_{tex} and only train the feature encoder f_{enc} as well as the NeRF MLP f_{nf} . Conveniently, NeRF can be supervised with masked multi-view images of the actor. Assuming C images of calibrated cameras for a fixed frame are given, a random foreground pixel r from a random camera is chosen, which has the ground truth color c_{gt}^r . We employ an ℓ_1 loss between the ground truth pixel color and the estimated one

$$\mathcal{L}_{color}(\tilde{c}^r) = \|\tilde{c}^r - c_{gt}^r\|_1 \quad (14)$$

where \tilde{c}^r is obtained according to Equation 7 and 13.

3.3 NeRF-guided Deformation Refinement

So far, we have discussed how the NeRF representation can leverage the advantages of the underlying 3D template mesh. However, the geometry can also be improved using the neural radiance field. The key observation is that a weakly supervised setup, as proposed by [Habermann et al. 2021], struggles with recovering the finer wrinkles on the clothing (see Figure 4). This is mostly due to the limited supervision from the rendering losses, i.e. \mathcal{L}_{sil} and \mathcal{L}_{chroma} . For the silhouette loss \mathcal{L}_{sil} , the main limiting factor is that it can at most recover details up to the visual hull, which is carved into the 3D volume by the multi-view foreground masks. For the dense rendering loss \mathcal{L}_{chroma} , there are three limitations: 1) the rendering loss is very sensitive to local minima as gradients of the input image are computed with finite differences on the ground truth image; 2) this loss struggles with deformations that are out of the camera plane, and 3) the rendering loss cannot account for shadows and view-dependent effects. A possible solution is to further improve the rendering loss by using ray-tracing based approaches that are differentiable [Li et al. 2018; Nimier-David et al. 2019] or shadow-aware rasterizers [Lyu et al. 2021]. However, their runtime is rather slow or the approximations are too coarse for humanoid subjects, which prevents them from being used in this setup. Fortunately, it can be observed that the per-view pointclouds that can be recovered from the proposed NeRF architecture contain small-scale wrinkles (see Figure 4), which cannot be recovered by recent weakly-supervised approaches [Habermann et al. 2021, 2020]. Thus, we propose to supervise the template mesh by a 3D-to-3D constraint between the posed and deformed template and the per-view pointcloud, which has the advantage that no explicit per-frame multi-view stereo reconstruction is required as a separate step.

3.3.1 Pointcloud Extraction. First, the per-view pointcloud for any given ray r from any given camera of the current frame can be computed as

$$p^r = o^r + \left(\sum_{i=0}^K T_i^r \alpha_i^r t_i^r(V) \right) d^r. \quad (15)$$

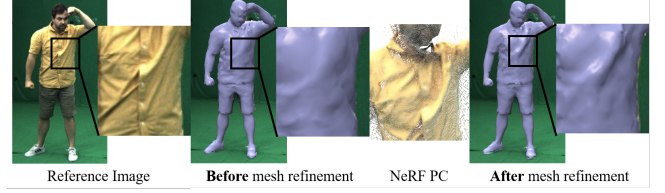


Fig. 4. Here, we visualize the influence of the NeRF-guided geomtry refinement using the proposed pointcloud loss. Note that the NeRF pointcloud contains much more geometric detail than the mesh *before refinement*. Once we refined f_{delta} using the view-dependent pointcloud, these geometric details are also contained in the deformed mesh.

Here, we use our mesh-guided NeRF representation (Equation 13) and volume rendering (Equation 8 and 9) to acquire the density per ray sample i . This density is used to weight each (depth) sample along the ray and returns the average depth, which is then multiplied with the viewing direction d^r . Adding the camera origin o^r leads to the final point p^r in global 3D space. We only sample rays for pixels where the dilated depth map is non-zero (foreground pixels). For each frame and view, we sample $R = 8192$ points, which we found is a good compromise between accuracy and training speed.

3.3.2 Mesh Deformation Refinement. Now, the goal is to further refine the mesh deformation network f_{delta} while keeping the embedded deformation network f_{eg} fixed. In detail, we refine the network using an additional loss

$$\begin{aligned} \mathcal{L}_{pc}(V) = & \sum_{j=0}^N \eta \left(\min_{r \in \{0, \dots, R\}} \|V_j - p^r\|^2 \right) \\ & + \sum_{r=0}^R \eta \left(\min_{j \in \{0, \dots, N\}} \|p^r - V_j\|^2 \right) \end{aligned} \quad (16)$$

where N is the number of template vertices and $\eta(\cdot)$ is a robust loss function that sets the value to zero when it exceeds a certain threshold $T = 4cm$ to ensure robustness with respect to outliers. Now, DeltaNet is refined with the losses

$$\mathcal{L}_{mesh} = \mathcal{L}_{pc} + \mathcal{L}_{sil} + \mathcal{L}_{laplacian} + \mathcal{L}_{edge}. \quad (17)$$

Here, \mathcal{L}_{edge} is an isometry or edge length constraint that is imposed similar to the one proposed by [Habermann et al. 2019]. This constraint has the advantage that it allows local rotations in contrast to Laplacian regularization, which is important when trying to reproduce wrinkle patterns. \mathcal{L}_{sil} and $\mathcal{L}_{laplacian}$ are a multi-view silhouette loss and a Laplacian regularizer [Habermann et al. 2021]. Note that we assign the Laplacian regularizer a very low weight (see supplemental document) to ensure that wrinkles beyond the ones in the template can be modeled. However, not using a Laplacian regularization at all leads to spikes in the results. Therefore, we use this combination of spatial regularizers. Figure 4 shows that the proposed NeRF pointcloud loss can help to recover finer wrinkles in the geometry, to remove baked-in template wrinkles, and to ensure that the deformed and posed template better matches the ground truth.

Once the mesh is refined, the whole process can be iterated (starting again from Section 3.2). We found that the refined geometry

further improves the synthesis quality, which ultimately means that a synergy effect between the deformable mesh and the neural radiance field arises and both improve each other over each iteration till convergence is reached.

3.4 Training Procedure

We first train f_{enc} and f_{inf} . Once trained, we refine the deformation network using the NeRF-guided loss. Then, we use the refined geometry to train f_{enc} and f_{inf} once more, first on the lower resolution images and later on the $4k$ images. This procedure could potentially be iterated multiple times, but we found that in practice a single iteration is sufficient. All our experiments are performed on a machine with 2 to 4 NVIDIA Quadro RTX 8000 48Gb graphics cards and an AMD EPYC 7502P 32-Core processing unit. For each subject, the training of the NeRF MLP and the texture encoder leverages 2 GPUs and takes about 9 days. Refining the surface deformation network also leverages 2 GPUs and takes 1.5 days. The training of the texture translation network requires 4 GPUs and takes 7 days. However, this step can be trained in parallel since the NeRF MLP and the texture encoder leverage the ground truth textures during training. Thus, the total training time is around 10 days. At test time, our approach requires around 12 seconds to generate a 4K image using a single GPU.

4 RESULTS

Next, we provide the details for the dataset, show qualitative and quantitative results, and compare our approach to other methods and baselines. For more results, we refer to our supplemental video.

Dataset. To evaluate the proposed approach, we leverage the publicly available *DynaCap*¹ dataset [Habermann et al. 2021], which contains 5 different actors recorded (using between 50 and 101 cameras each) for around 20k training frames and 5k testing frames. Three actors wear loose clothes, i.e., two dresses and one skirt. The other two actors wear tighter clothing, i.e., short and long pants and long and short sleeves. Each actor is performing a large variety of motions for the training and testing sequences. Further, the motions in the test split significantly differ from the ones contained in the training set. If not mentioned otherwise, we leverage all available cameras for training. We follow the proposed train/test split of the dataset. The original released dataset has an image resolution of 1285×940 . However, the authors of the dataset also provided us the full resolution videos (4112×3008) for all sequences.

4.1 Qualitative Results

First, we show qualitative results for the image synthesis quality of our approach in Figure 5 for all subjects in the dataset. We visualize novel view synthesis results for training motions (left column) as well as novel motion and view results (right column) and provide a reference image for each actor. Note that in both modes, the results look highly photorealistic and even small clothing wrinkles can be realistically synthesized. View-dependent appearance effects, such as view-dependent specular highlights on the skin of the actors, are also synthesized realistically. Notably, our method consistently

achieves a high synthesis quality irrespective of the clothing type such that even loose clothing can be synthesized well.

In addition, we show qualitative results of our space-time coherent geometry reconstructions (on the training motions) and synthesized motion-dependent deformations (on the testing motions) in Figure 6. Note that 3D wrinkle patterns can be nicely recovered in the geometry and the mesh also aligns well to the reference views even though our method does not take these images as input.

These results demonstrate that our method is very versatile in the sense that it is able to 1) faithfully reconstruct the geometry of the training sequence and to 2) re-render the training sequences from novel views. Moreover, our method is also capable of 3) synthesizing motion-dependent surface deformations for unseen skeletal motions and 4) synthesizing photo-real images of the actor performing these unseen skeletal motions.

4.2 Comparisons to the State of the Art

Next, we compare our approach to the state of the art. We first explain the evaluation setup, introduce the previous works we compare to, the evaluation metrics, and finally report the results of the performed evaluations.

4.2.1 Evaluation Sequence. We compare to other methods on the challenging *D2* sequence of the *DynaCap* dataset in which the subject is wearing short pants and a short sleeve. Note that we do not evaluate on subjects with more loose clothing as except Habermann et al. [2021] and our method no previous work is able to track loose clothing. The motions that are performed in this recording range from simple walking motions to very challenging and fast motions such as boxing and dancing. Every metric is averaged across the entire sequence using every 10th frame. We hold out four cameras (with indices 7, 18, 27, and 40) for testing, which are uniformly sampled in space. For quantitative evaluation, we also reconstruct pseudo ground truth geometry per frame using an off-the-shelf multi-view stereo reconstruction software [Agisoft 2016].

4.2.2 Previous Methods and Baselines. We compare to Neural Actor (NA) [Liu et al. 2021] and A-NeRF [Su et al. 2021], which are also hybrid approaches in the sense that they attach a NeRF to a naked human body model [Loper et al. 2015] or skeleton. We further compare to Neural Volumes (NV) [Lombardi et al. 2019], which is a neural volume rendering approach and Neural Body (NB) [Peng et al. 2021b], which leverages structured latent codes that can be posed using an underlying skeleton structure. We also compare to the surface and neural texture-based approach, Deep Dynamic Character (DDC) [Habermann et al. 2021], which is the only related work that also tracks and synthesizes the underlying surface deformation. Last, we compare to Neural Human Renderer (NHR) [Wu et al. 2020], which uses a point-based scene representation.

4.2.3 Metrics. To measure image synthesis quality, we first mask all results using the eroded ground truth foreground masks since even ground truth masks still contain segmentation errors. Otherwise falsely classified background pixels, that are however correctly recovered by the respective methods would erroneously lead to high errors. Then, we evaluate the peak signal-to-noise ratio (PSNR).

¹All data captures and evaluations were performed at MPII by MPII.



Fig. 5. Qualitative results of our method on the *DynaCap* dataset. We show qualitative results for novel views and for novel skeletal motions, which were not seen during training. Note that our method achieves a photo-realistic rendering quality and even individual clothing wrinkles appear sharp in the images. Importantly, in contrast to other recent hybrid approaches that leverage neural radiance fields, our method is able to also synthesize subjects wearing loose types of apparel such as skirts and dresses.

However, this metric does not reflect the visual perception of humans, i.e., blurry results can have a low error although they appear very unrealistic to the human eye [Zhang et al. 2018]. Hence, we also report the learned perceptual image patch similarity (LPIPS) [Zhang et al. 2018], and the Fréchet inception distance (FID) [Heusel et al. 2017] metrics, which are human perception-based metrics. In contrast to our approach, other methods cannot generate results at

4K resolution (4112×3008) in a reasonable time, we evaluate all metrics on the downsampled versions (1285×940) if not specified otherwise. To measure geometry quality, we report the Chamfer distance between the pseudo ground truth and the reconstructed results as well as the Hausdorff distance computed from the result to the ground truth.



Fig. 6. Qualitative results showing our reconstructed/synthesized geometry on the *DynaCap* dataset. Note that due to the novel NeRF-guided supervision of surface deformations, geometric details (such as clothing wrinkles) can be recovered nicely. Further, the surface reconstruction of training motions as well as the surface synthesis, both, look plausible when overlaid onto the reference images. In both settings, the images are *not* an input to our method.

4.2.4 Image Synthesis Accuracy. First, we evaluate the image synthesis quality of our approach and compare it to previous works. In Figure 7, we show a qualitative comparison to previous works. For NB [Peng et al. 2021b], NV [Lombardi et al. 2019], and NHR [Wu et al. 2020], the results are very blurry and contain obvious visual artifacts. Compared to their original results, we found that when using the larger and more challenging *DynaCap* training dataset, which also contains more variations, the quality of these methods significantly degrades. Thus, these methods seem to be inherently limited to shorter sequences and exhibit limited generalization ability in

terms of unseen poses and views. The results of DDC [Habermann et al. 2021] are less blurry compared to the aforementioned methods, but high frequency wrinkles are still not recovered well. In contrast, NA [Liu et al. 2021] captures such wrinkles, but as mentioned earlier this work can only handle tight types of clothing. In contrast to that, our method is able to synthesize arbitrary types of apparel and also produces the sharpest and most detailed results. We refer to the supplemental video for a more detailed comparison. These findings can be observed for the novel view synthesis as well as for the motion synthesis task.

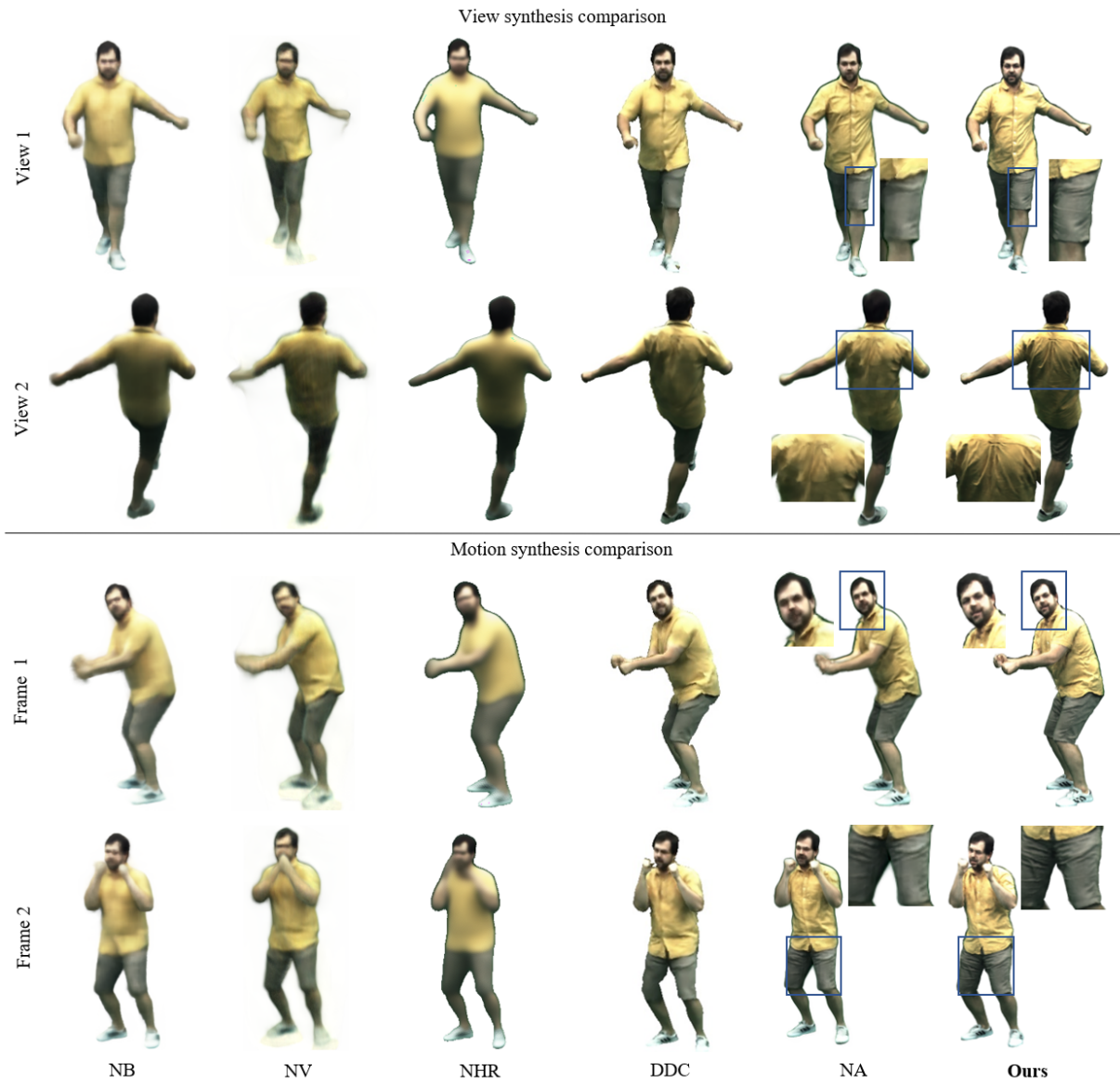


Fig. 7. Here, we visually compare our approach in terms of the image synthesis quality to two recent neural human rendering methods, Neural Actor [Liu et al. 2021], and Deep Dynamic Characters [Habermann et al. 2021]. Note that our approach renders sharper images and smaller details in the image can be much better recovered by our method compared to the previous works. This can be observed for the novel view synthesis task as well as for the motion synthesis task. Zoom in to better see the qualitative differences.

Table 1 also quantitatively confirms that our method achieves the best view synthesis results in terms of perceptual metrics. For a fair comparison, we provide the numbers for our method when we did *not* use 4K videos during training (referred to as *Ours w/o 4k*). Importantly, other methods cannot be trained on 4K video data in a reasonable amount of time while our method design allows training on such data in general. Notably, we outperform other approaches in terms of LPIPS and FID by 27.2% and 73.4%, respectively. The difference in PSNR however is less prominent since this metric is less sensitive to blurry results and, thus, even if results are more blurry

the PSNR can be higher. This explains why DDC has a slightly better score even though our results are significantly more plausible. Again, it is worth mentioning that the PSNR metric is not fully indicative of visual quality and results can have a low error although these images appear less realistic to the human eye [Zhang et al. 2018]. As stated in Section 3.2.1, we found that the motion to appearance mapping is an one-to-many mapping, i.e. the same motion can lead to slightly different wrinkle patterns, which is in line with the findings of other works [Bagautdinov et al. 2021; Liu et al. 2021]. While others [Habermann et al. 2021; Lombardi et al. 2019; Peng et al.

Table 1. View synthesis error of the *D1* sequence. Here, we evaluate the view synthesis quality of our approach and compare it to previous works. Note that we achieve by far the highest scores for the perception-based metrics and also in terms of PSNR our method performs better than the previous state-of-the-art methods.

View synthesis error on <i>D2</i>			
Method	PSNR \uparrow	LPIPS \downarrow ($\times 1000$)	FID \downarrow
NB	29.94	42.15	109.98
NV	25.49	85.69	123.19
NHR	28.39	46.07	116.59
DDC	32.96	20.07	27.73
NA	30.21	23.60	18.56
A-NeRF	29.54	35.27	86.90
Ours w/o 4k	31.00	14.61	4.93
Ours w/ GT textures	33.96	10.87	5.15
Ours w/o ref. and 4k	29.89	17.63	8.54
Ours (4112 \times 3008)	29.32	43.87	11.26
Ours w/o 4k (4112 \times 3008)	29.11	46.11	12.82

2021b; Su et al. 2021; Wu et al. 2020] ignore this, we explicitly account for it by leveraging a discriminator during the training of the texture network. Thus, our generated textures are sharp and plausible, but the exact wrinkles might vary from the ground truth since there is no unique mapping. In our final rendering, such variations in the wrinkles look highly realistic (confirmed by our improvement in terms of perceptual metrics), but they will not fully align with the ground truth resulting in a lower PSNR compared to a blurred result. To confirm this, we also evaluate our method when using the ground truth texture maps instead of the synthesized texture map such that wrinkles in the texture align with the real ones, referred to as *Ours w/ GT textures*. One can notice that the PSNR then outperforms previous works, which confirms our hypothesis.

The same tendency can be observed when comparing to other works in terms of motion synthesis (see Table 2). Again, our method achieves the best perceptual results due to the high quality synthesis of our approach. In terms of PSNR, some methods achieve a higher score although results are notably very blurred and/or not photo-real. The reason is the same as before, which also for this setting can be confirmed when evaluating the PSNR value for *Ours w/ GT textures*. However, as confirmed by our qualitative results and the supplemental video, our method clearly outperforms previous works in terms of perceived image quality, plausibility, and photorealism.

4.2.5 Geometry Deformation Accuracy. In Figure 8, Table 3, and Table 4, we qualitatively and quantitatively evaluate the surface deformation accuracy of our approach and compare it to DDC [Habermann et al. 2021] and NA Liu et al. [2021]. For NA, we used Marching Cubes to retrieve per-frame reconstructions from the NeRF-based density field. The recovered geometries contain a lot of noise since the density field is not regularized, thus, resulting in a worse performance compared to our method. DDC is the only previous work that also tracks the space-time coherent deformation of the template. One can see that our method has an overall lower error in terms of surface quality, which is due to our NeRF-guided supervision.

Table 2. Moreover, we also evaluate the motion synthesis quality of our approach and compare it previous methods. Again, we outperform other works in terms of the perception-based metrics and are comparable to earlier works in terms of PSNR.

Motion synthesis error on <i>D2</i>			
Method	PSNR \uparrow	LPIPS \downarrow ($\times 1000$)	FID \downarrow
NB	29.37	43.99	115.70
NV	23.32	98.35	139.82
NHR	28.08	47.65	122.60
DDC	28.05	30.43	38.37
NA	28.43	28.33	24.50
A-NeRF	28.42	38.74	95.56
Ours w/o 4k	27.69	24.0	9.25
Ours w/ GT textures	31.32	15.84	9.34
Ours w/o ref. and 4k	27.49	25.64	12.90
Ours (4112 \times 3008)	26.04	49.81	15.13
Ours w/o 4k (4112 \times 3008)	26.02	50.38	16.21

Table 3. Here, we evaluate the 3D error on the training skeletal motion of the *D2* sequence. Note that the proposed method outperforms previous work in terms of tracking the surface deformation. The error is reported in *cm*.

Reconstruction Error on <i>D2</i>		
Method	Chamfer \downarrow	Hausdorff \downarrow
NA	2.21	2.75
DDC	1.2686	1.1922
Ours w/o 4k	1.0071	0.8872

Table 4. We evaluate the 3D error on the test skeletal motion of the challenging *D2* sequence. Note that the proposed method outperforms previous work in terms of deformation synthesis. The error is reported in *cm*.

Deformation generation error on <i>D2</i>		
Method	Chamfer \downarrow	Hausdorff \downarrow
NA	2.29	2.82
DDC	1.43	1.38
Ours w/o 4k	1.24	1.15

DDC in contrast only learns the deformations from image-based supervision signals, thus leading to baked-in wrinkles from the base template, which cannot be removed. Further, new wrinkle patterns, which appear while the actor is performing different motions, cannot be tracked well by DDC, i.e., the wrinkles in the geometry often do not match the ones in the images as indicated by the red boxes in Figure 8. In contrast, we demonstrate that our NeRF guidance helps the deforming geometry to recover these details.

4.3 Ablation Studies

Next, we study the individual design choices of our approach.

4.3.1 Deformable Mesh Guidance. First, we evaluate the design choice of uniting an explicit and *deformable* mesh representation

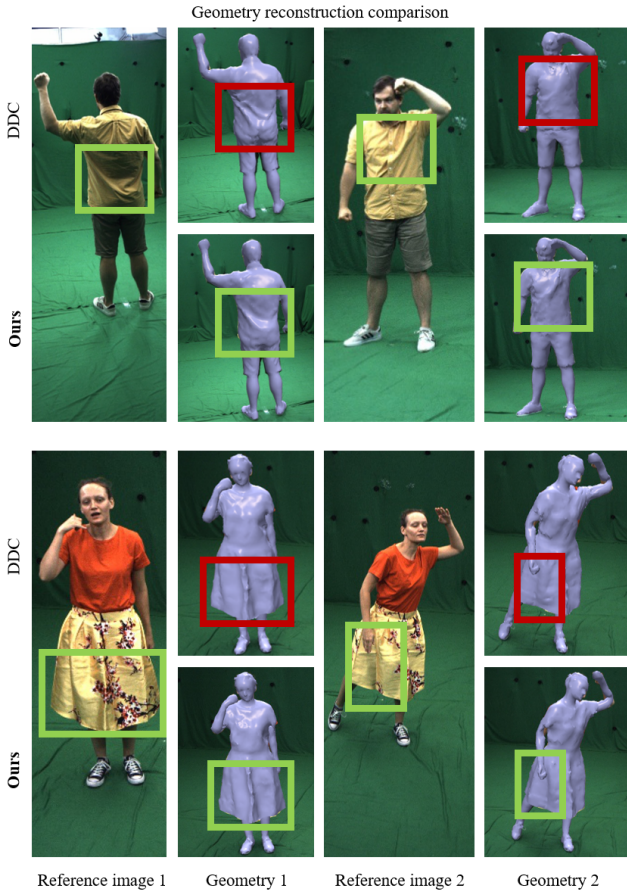


Fig. 8. We also compare the surface deformation quality of our approach to previous work [Habermann et al. 2021]. Due to our NeRF-guided supervision, geometric details can be better tracked compared to the other method, which solely supervises the geometry in image space. Thus, their recovered geometry suffers from baked-in wrinkles of the template mesh and wrinkles that are actually present in the images can be tracked less well compared to our approach.

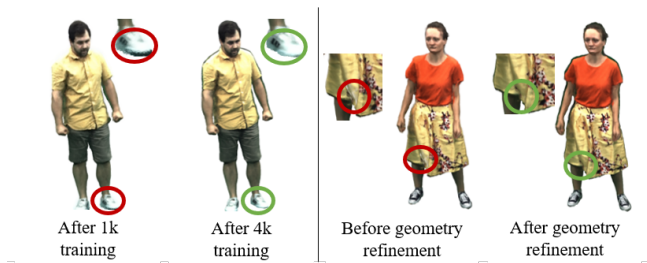


Fig. 9. Ablation study. We evaluate the effect of the 4k (4112×3008) image supervision with using only 1k (1285×940). Especially when zooming in, the 4k resolution shows a superior quality and image details are much sharper compared to only training on 1k images. Further, we evaluate the influence of the geometry refinement on the synthesis quality. Note that a better deformation tracking also greatly improves the synthesis quality.

with a neural radiance field. To this end, we leverage the pre-trained deformation networks of DDC [Habermann et al. 2021] to obtain the deformed geometry and apply our mesh-guided radiance field (Section 3.2); this method is referred to as *Ours w/o ref. and 4k* in Table 1 and 2. Note that we show a consistent improvement in terms of perceptual metrics over NA [Liu et al. 2021] and DDC [Habermann et al. 2021]. NA can be considered as a method that leverages an explicit *piece-wise rigid* mesh to guide a neural radiance field. In contrast, DDC explicitly accounts for non-rigid mesh deformations, but it does not leverage a NeRF representation. Thus, this baseline comparison clearly shows the advantage of uniting a *deformable* mesh representation with a neural radiance field.

4.3.2 Geometry Refinement. Next, we evaluate the influence of the NeRF-guided geometry refinement (Section 3.3). In Figure 9, we show how the better geometry tracking helps to achieve a higher synthesis quality as wrinkle patterns appear sharper. This is also quantitatively confirmed in Table 1 and 2 where the result with our proposed refinement (*Ours w/o 4k*) is consistently better than our result without refinement (*Ours w/o ref. and 4k*). In terms of geometry error, we found that compared to the baseline (DDC), the NeRF-guided loss also helps to recover geometry that is closer to the ground truth (see Table 3 and 4). Thus, for both tasks, image synthesis and surface recovery, the proposed NeRF-guided geometry refinement improves the results. Importantly, the joint consideration of deformation tracking and synthesis, for the first time, allows to achieve such photo-real quality for *loose types of apparel*.

4.3.3 4K Supervision. We further study the influence of the 4k image resolution in Figure 9. Again, one can see that more details in the image can be preserved when 4k images are used for training, i.e., the black stripes on the shoe are sharper. This is also quantitatively confirmed in the last two rows of Table 1 and 2 where we evaluate the metrics on the *higher resolution* (4112×3008) images instead of the downsampled ones. Note that the error can be further reduced by using the 4K supervision and that training on such data is only possible in an acceptable time due to our more efficient mesh-based sampling and feature attachment strategy. In fact, the original NeRF architecture (using the fine MLP as well) requires $64 + 128$ samples per ray whereas our proposed architecture and sampling only requires 32 samples. This in fact reduces our training time to 10 days compared to 29 days when using the original architecture.

5 CONCLUSION

We proposed HDHumans a method for view and motion synthesis of digital human characters from multi-view videos. Our method solely takes a skeletal motion and a camera pose and produces high resolution images and videos of an unprecedented quality. At the technical core, we propose to jointly learn the surface deformation of the human and the appearance in form of a neural radiance field. We showed that this has a synergy effect and the combination of both scene representations improves each other. Our results demonstrate that our method is a clear step forward towards more photo-realistic and higher resolution digital avatars, which will be an important part for the upcoming era of AR and VR. We also believe that our work can be a solid basis for future research in this direction, which

potentially tackles the challenges of real-time compute, relighting, and face and hand gesture synthesis.

ACKNOWLEDGMENTS

All data captures and evaluations were performed at MPII by MPII. The authors from MPII were supported by the ERC Consolidator Grant 4DRepLy (770784), the Deutsche Forschungsgemeinschaft (Project Nr. 409792180, Emmy Noether Programme, project: Real Virtual Humans) and Lise Meitner Postdoctoral Fellowship.

REFERENCES

- Kfir Aberman, Mingyi Shi, Jing Liao, Dani Lischinski, Baoquan Chen, and Daniel Cohen-Or. 2019. Deep Video-Based Performance Cloning. *Comput. Graph. Forum* 38, 2 (2019), 219–233. <https://doi.org/10.1111/cgf.13632>
- Agisoft. 2016. PhotoScan. <http://www.agisoft.com>.
- Thiemo Alldieck, Marcus Magnor, Weipeng Xu, Christian Theobalt, and Gerard Pons-Moll. 2018. Video Based Reconstruction of 3D People Models. *2018 IEEE/CVF Conference on Computer Vision and Pattern Recognition* 1, 1 (2018), 8387–8397. <https://doi.org/10.1109/CVPR.2018.00875>
- Anonymous. 2022. Neural Novel Actor: Learning Generalizable Neural Radiance Field for Human Actors with Pose Control. (2022).
- Timur Bagautdinov, Chenglei Wu, Tomas Simon, Fabián Prada, Takaaki Shiratori, Shih-En Wei, Weipeng Xu, Yaser Sheikh, and Jason Saragih. 2021. Driving-Signal Aware Full-Body Avatars. *ACM Trans. Graph.* 40, 4, Article 143 (jul 2021), 17 pages. <https://doi.org/10.1145/3450626.3459850>
- Joel Carranza, Christian Theobalt, Marcus A. Magnor, and Hans-Peter Seidel. 2003. Free-viewpoint Video of Human Actors. *ACM Trans. Graph.* 22, 3 (July 2003).
- Dan Casas, Marco Volino, John Collomosse, and Adrian Hilton. 2014. 4D Video Textures for Interactive Character Appearance. *Comput. Graph. Forum* 33, 2 (May 2014), 0.
- Caroline Chan, Shiry Ginossar, Tinghui Zhou, and Alexei A Efros. 2019. Everybody Dance Now. *IEEE International Conference on Computer Vision (ICCV)* 1 (2019), 0–0.
- Eric R. Chan, Connor Z. Lin, Matthew A. Chan, Koki Nagano, Boxiao Pan, Shalini De Mello, Orazio Gallo, Leonidas Guibas, Jonathan Tremblay, Sameh Khamis, Tero Karras, and Gordon Wetzstein. 2022. Efficient Geometry-aware 3D Generative Adversarial Networks. In *CVPR*.
- Jianchuan Chen, Ying Zhang, Di Kang, Xuefei Zhe, Linchao Bao, and Huchuan Lu. 2021. Animatable Neural Radiance Fields from Monocular RGB Video. <arXiv:2106.13629> [cs.CV]
- Alvaro Collet, Ming Chuang, Pat Sweeney, Don Gillett, Dennis Evseev, David Calabrese, Hugues Hoppe, Adam Kirk, and Steve Sullivan. 2015. High-quality streamable free-viewpoint video. *ACM Transactions on Graphics (TOG)* 34, 4 (2015), 69.
- Terrance DeVries, Miguel Angel Bautista, Nitish Srivastava, Graham W. Taylor, and Joshua M. Susskind. 2021. Unconstrained Scene Generation with Locally Conditioned Radiance Fields. *arXiv* (2021).
- Fridovich-Keil and Yu, Matthew Tancik, Qinhong Chen, Benjamin Recht, and Angjoo Kanazawa. 2022. Plenoxels: Radiance Fields without Neural Networks. In *CVPR*.
- Guy Gafni, Justus Thies, Michael Zollhöfer, and Matthias Nießner. 2021. Dynamic Neural Radiance Fields for Monocular 4D Facial Avatar Reconstruction. In *Proceedings of the IEEE/CVF Conference on Computer Vision and Pattern Recognition (CVPR)*, 8649–8658.
- Stephan J. Garbin, Marek Kowalski, Matthew Johnson, Jamie Shotton, and Julien Valentin. 2021. FastNeRF: High-Fidelity Neural Rendering at 200FPS. In *Proceedings of the IEEE/CVF International Conference on Computer Vision (ICCV)*, 14346–14355.
- A. K. Grigor'ev, Artem Sevastopolsky, Alexander Vakhitov, and Victor S. Lempitsky. 2019. Coordinate-Based Texture Inpainting for Pose-Guided Human Image Generation. *Computer Vision and Pattern Recognition (CVPR)* (2019), 12127–12136.
- Marc Habermann, Lingjie Liu, Weipeng Xu, Michael Zollhoefer, Gerard Pons-Moll, and Christian Theobalt. 2021. Real-Time Deep Dynamic Characters. *ACM Trans. Graph.* 40, 4, Article 94 (jul 2021), 16 pages. <https://doi.org/10.1145/3450626.3459749>
- Marc Habermann, Weipeng Xu, Michael Zollhoefer, Gerard Pons-Moll, and Christian Theobalt. 2020. DeepCap: Monocular Human Performance Capture Using Weak Supervision. *Proceedings of the Conference on Computer Vision and Pattern Recognition (CVPR)* 1 (2020), 1.
- Marc Habermann, Weipeng Xu, Michael Zollhöfer, Gerard Pons-Moll, and Christian Theobalt. 2019. LiveCap: Real-Time Human Performance Capture From Monocular Video. *ACM Transactions on Graphics (TOG)* 38, 2, Article 14 (2019), 17 pages. <https://doi.org/10.1145/3311970>
- Kaiming He, Xiangyu Zhang, Shaoqing Ren, and Jian Sun. 2016. Deep Residual Learning for Image Recognition. *2016 IEEE Conference on Computer Vision and Pattern Recognition (CVPR)* 1, 1 (2016), 770–778. <https://doi.org/10.1109/CVPR.2016.90>
- Peter Hedman, Pratul P. Srinivasan, Ben Mildenhall, Jonathan T. Barron, and Paul Debevec. 2021. Baking Neural Radiance Fields for Real-Time View Synthesis. *ICCV* (2021).
- Martin Heusel, Hubert Ramsauer, Thomas Unterthiner, Bernhard Nessler, and Sepp Hochreiter. 2017. GANs Trained by a Two Time-Scale Update Rule Converge to a Local Nash Equilibrium. In *Proceedings of the 31st International Conference on Neural Information Processing Systems* (Long Beach, California, USA) (NIPS'17). Curran Associates Inc., Red Hook, NY, USA, 6629–6640.
- Anna Hilsmann, Philipp Fechteler, Wieland Morgenstern, Wolfgang Paier, Ingo Feldmann, Oliver Schreer, and Peter Eisert. 2020. Going beyond free viewpoint: creating animatable volumetric video of human performances. *IET Computer Vision* 14, 6 (Sept. 2020).
- Phillip Isola, Jun-Yan Zhu, Tinghui Zhou, and Alexei A. Efros. 2017. Image-to-Image Translation with Conditional Adversarial Networks. *2017 IEEE Conference on Computer Vision and Pattern Recognition (CVPR)* 1, 1 (2017), 5967–5976. <https://doi.org/10.1109/CVPR.2017.632>
- Zhang Jiakai, Liu Xinhang, Ye Xinyi, Zhao Fuqiang, Zhang Yanshun, Wu Minye, Zhang Yingliang, Xu Lan, and Yu Jingyi. 2021. Editable Free-Viewpoint Video using a Layered Neural Representation. In *ACM SIGGRAPH*.
- Moritz Kappel, Vladislav Golyanik, Mohamed Elgharib, Jann-Ole Henningson, Hans-Peter Seidel, Susana Castillo, Christian Theobalt, and Marcus Magnor. 2020. High-Fidelity Neural Human Motion Transfer from Monocular Video. <arXiv:2012.10974> [cs.CV]
- Diederik Kingma and Jimmy Ba. 2014. Adam: A Method for Stochastic Optimization. *International Conference on Learning Representations* (12 2014).
- Youngjoong Kwon, Dahun Kim, Duygu Ceylan, and Henry Fuchs. 2021. Neural Human Performer: Learning Generalizable Radiance Fields for Human Performance Rendering. *NeurIPS* (2021).
- Marc Levoy. 1990. Efficient Ray Tracing of Volume Data. *ACM Trans. Graph.* 9, 3 (July 1990), 245–261. <https://doi.org/10.1145/78964.78965>
- Guannan Li, Yebin Liu, and Qionghai Dai. 2014. Free-viewpoint Video Relighting from Multi-view Sequence Under General Illumination. *Mach. Vision Appl.* 25, 7 (Oct. 2014), 1737–1746. <https://doi.org/10.1007/s00138-013-0559-0>
- Tzu-Mao Li, Miika Aittala, Frédo Durand, and Jaakko Lehtinen. 2018. Differentiable Monte Carlo Ray Tracing through Edge Sampling. *ACM Trans. Graph. (Proc. SIGGRAPH Asia)* 37, 6 (2018), 222:1–222:11.
- Yining Li, Chen Huang, and Chen Change Loy. 2019. Dense Intrinsic Appearance Flow for Human Pose Transfer. In *IEEE Conference on Computer Vision and Pattern Recognition*.
- Z. Li, Simon Niklaus, Noah Snively, and Oliver Wang. 2020. Neural Scene Flow Fields for Space-Time View Synthesis of Dynamic Scenes. *ArXiv abs/2011.13084* (2020).
- Lingjie Liu, Jiatao Gu, Kyaw Zaw Lin, Tat-Seng Chua, and Christian Theobalt. 2020a. Neural Sparse Voxel Fields. *NeurIPS* (2020).
- Lingjie Liu, Marc Habermann, Viktor Rudnev, Kripasindhu Sarkar, Jiatao Gu, and Christian Theobalt. 2021. Neural Actor: Neural Free-View Synthesis of Human Actors with Pose Control. *ACM Trans. Graph.* 40, 6, Article 219 (dec 2021), 16 pages. <https://doi.org/10.1145/3478513.3480528>
- Lingjie Liu, Weipeng Xu, Marc Habermann, Michael Zollhöfer, Florian Bernard, Hyeonwoo Kim, Wenping Wang, and Christian Theobalt. 2020b. Neural Human Video Rendering by Learning Dynamic Textures and Rendering-to-Video Translation. *Transactions on Visualization and Computer Graphics (TVCG)* PP (2020), 1–1. <https://doi.org/10.1109/TVCG.2020.2996594>
- Lingjie Liu, Weipeng Xu, Michael Zollhöfer, Hyeonwoo Kim, Florian Bernard, Marc Habermann, Wenping Wang, and Christian Theobalt. 2019b. Neural Rendering and Reenactment of Human Actor Videos. *ACM Transactions on Graphics (TOG)* 38, 5, Article 139 (2019), 14 pages. <https://doi.org/10.1145/3333002>
- Wen Liu, Zhixin Piao, Jie Min, Wenhan Luo, Lin Ma, and Shenghua Gao. 2019a. Liquid warping gan: A unified framework for human motion imitation, appearance transfer and novel view synthesis. In *Proceedings of the IEEE/CVF International Conference on Computer Vision*. 5904–5913.
- Stephen Lombardi, Tomas Simon, Jason Saragih, Gabriel Schwartz, Andreas Lehrmann, and Yaser Sheikh. 2019. Neural volumes: Learning dynamic renderable volumes from images. *ACM Transactions on Graphics (TOG)* 38, 4 (2019), 65.
- Stephen Lombardi, Tomas Simon, Gabriel Schwartz, Michael Zollhoefer, Yaser Sheikh, and Jason Saragih. 2021. Mixture of Volumetric Primitives for Efficient Neural Rendering. <arXiv:2103.01954> [cs.GR]
- Matthew Loper, Naureen Mahmood, Javier Romero, Gerard Pons-Moll, and Michael J. Black. 2015. SMPL: A Skinned Multi-Person Linear Model. *ACM Trans. Graphics (Proc. SIGGRAPH Asia)* 34, 6 (Oct. 2015), 248:1–248:16.
- Linjie Lyu, Marc Habermann, Lingjie Liu, Mallikarjun B R, Ayush Tewari, and Christian Theobalt. 2021. Efficient and Differentiable Shadow Computation for Inverse Problems. In *Proceedings of the International Conference on Computer Vision (ICCV)* 1 (2021), 1.
- Liqian Ma, Xu Jia, Qianru Sun, Bernt Schiele, Tinne Tuytelaars, and Luc Van Gool. 2017. Pose guided person image generation. In *Advances in Neural Information Processing Systems*. 405–415.
- Liqian Ma, Qianru Sun, Stamatios Georgoulis, Luc van Gool, Bernt Schiele, and Mario Fritz. 2018. Disentangled Person Image Generation. *Computer Vision and Pattern Recognition (CVPR)* (2018).

- Ben Mildenhall, Pratul P. Srinivasan, Matthew Tancik, Jonathan T. Barron, Ravi Ramamoorthi, and Ren Ng. 2020. NeRF: Representing Scenes as Neural Radiance Fields for View Synthesis. In *Computer Vision – ECCV 2020*, Andrea Vedaldi, Horst Bischof, Thomas Brox, and Jan-Michael Frahm (Eds.). Springer International Publishing, Cham, 405–421.
- Natalia Neverova, Riza Alp Güler, and Iasonas Kokkinos. 2018. Dense Pose Transfer. *European Conference on Computer Vision (ECCV)* (2018).
- Michael Niemeyer, Lars Mescheder, Michael Oechsle, and Andreas Geiger. 2020. Differentiable Volumetric Rendering: Learning Implicit 3D Representations without 3D Supervision. In *Proc. IEEE Conf. on Computer Vision and Pattern Recognition (CVPR)*.
- Merlin Nimier-David, Delio Vicini, Tizian Zeltner, and Wenzel Jakob. 2019. Mitsuba 2: A Retargetable Forward and Inverse Renderer. *ACM Trans. Graph.* 38, 6, Article 203 (Nov. 2019), 17 pages. <https://doi.org/10.1145/3355089.3356498>
- Atsuhiko Noguchi, Xiao Sun, Stephen Lin, and Tatsuya Harada. 2021. Neural Articulated Radiance Field. In *International Conference on Computer Vision*.
- Michael Oechsle, Songyou Peng, and Andreas Geiger. 2021. UNISURF: Unifying Neural Implicit Surfaces and Radiance Fields for Multi-View Reconstruction. In *International Conference on Computer Vision (ICCV)*.
- Keunhong Park, Utkarsh Sinha, Jonathan T. Barron, Sofien Bouaziz, Dan B Goldman, Steven M. Seitz, and Ricardo Martin-Brualla. 2020. Deformable Neural Radiance Fields. *arXiv preprint arXiv:2011.12948* (2020).
- Keunhong Park, Utkarsh Sinha, Peter Hedman, Jonathan T. Barron, Sofien Bouaziz, Dan B Goldman, Ricardo Martin-Brualla, and Steven M. Seitz. 2021. HyperNeRF: A Higher-Dimensional Representation for Topologically Varying Neural Radiance Fields. *ACM Trans. Graph.* 40, 6, Article 238 (dec 2021).
- Sida Peng, Junting Dong, Qianqian Wang, Shangzhan Zhang, Qing Shuai, Hujun Bao, and Xiaowei Zhou. 2021a. Animatable Neural Radiance Fields for Human Body Modeling. *ICCV* (2021).
- Sida Peng, Yuanqing Zhang, Yinghao Xu, Qianqian Wang, Qing Shuai, Hujun Bao, and Xiaowei Zhou. 2021b. Neural Body: Implicit Neural Representations with Structured Latent Codes for Novel View Synthesis of Dynamic Humans. *CVPR*, 1, 1 (2021), 9054–9063.
- Sergey Prokudin, Michael J. Black, and Javier Romero. 2021. SMPLpix: Neural Avatars from 3D Human Models. In *Winter Conference on Applications of Computer Vision (WACV)*. 1810–1819.
- Albert Pumarola, Antonio Agudo, Alberto Sanfeliu, and Francesc Moreno-Noguer. 2018. Unsupervised Person Image Synthesis in Arbitrary Poses. In *The IEEE Conference on Computer Vision and Pattern Recognition (CVPR)*.
- Albert Pumarola, Enric Corona, Gerard Pons-Moll, and Francesc Moreno-Noguer. 2020. D-NeRF: Neural Radiance Fields for Dynamic Scenes. *arXiv:2011.13961* [cs.CV]
- Amit Raj, Julian Tanke, James Hays, Minh Vo, Carsten Stoll, and Christoph Lassner. 2021. ANR: Articulated Neural Rendering for Virtual Avatars. In *IEEE/CVF Conference on Computer Vision and Pattern Recognition (CVPR)*.
- Christian Reiser, Songyou Peng, Yiyi Liao, and Andreas Geiger. 2021. KiloNeRF: Speeding up Neural Radiance Fields with Thousands of Tiny MLPs. In *International Conference on Computer Vision (ICCV)*.
- Kripasindhu Sarkar, Dushyant Mehta, Weipeng Xu, Vladislav Golyanik, and Christian Theobalt. 2020. Neural Re-Rendering of Humans from a Single Image. In *European Conference on Computer Vision (ECCV)*.
- Aliaksandra Shysheya, Egor Zakharov, Kara-Ali Aliev, Renat Bashirov, Egor Burkov, Karim Isakov, Aleksei Ivakhnenko, Yury Malkov, Igor Pasechnik, Dmitry Ulyanov, Alexander Vakhitov, and Victor Lempitsky. 2019. Textured Neural Avatars. In *The IEEE Conference on Computer Vision and Pattern Recognition (CVPR)*.
- Vincent Sitzmann, Michael Zollhöfer, and Gordon Wetzstein. 2019. Scene representation networks: Continuous 3D-structure-aware neural scene representations. In *Advances in Neural Information Processing Systems*. 1119–1130.
- Olga Sorkine and Marc Alexa. 2007. As-rigid-as-possible Surface Modeling. In *Proceedings of the Fifth Eurographics Symposium on Geometry Processing* (Barcelona, Spain) (SGP '07). Eurographics Association.
- Shih-Yang Su, Frank Yu, Michael Zollhoefer, and Helge Rhodin. 2021. A-NeRF: Surface-free Human 3D Pose Refinement via Neural Rendering. *arXiv preprint arXiv:2102.06199* (2021).
- Robert W. Sumner, Johannes Schmid, and Mark Pauly. 2007. Embedded Deformation for Shape Manipulation. *ACM Trans. Graph.* 26, 3 (July 2007).
- TheCaptury. 2020. The Captury. <http://www.thecaptury.com/>.
- Treedys. 2020. Treedys. <https://www.treedys.com/>.
- Edgar Tretschk, Ayush Tewari, Vladislav Golyanik, Michael Zollhöfer, Christoph Lassner, and Christian Theobalt. 2021. Non-Rigid Neural Radiance Fields: Reconstruction and Novel View Synthesis of a Dynamic Scene From Monocular Video. In *IEEE International Conference on Computer Vision (ICCV)*. IEEE.
- Marco Volino, Dan Casas, John Collomosse, and Adrian Hilton. 2014. Optimal Representation of Multiple View Video. In *Proceedings of the British Machine Vision Conference*. BMVA Press.
- Peng Wang, Lingjie Liu, Yuan Liu, Christian Theobalt, Taku Komura, and Wenping Wang. 2021. NeuS: Learning Neural Implicit Surfaces by Volume Rendering for Multi-view Reconstruction. *NeurIPS* (2021).
- Ting-Chun Wang, Ming-Yu Liu, Jun-Yan Zhu, Guilin Liu, Andrew Tao, Jan Kautz, and Bryan Catanzaro. 2018. Video-to-Video Synthesis. *Advances in Neural Information Processing Systems* 31 (2018). <https://proceedings.neurips.cc/paper/2018/file/d86ea612dec96096c5e0fcc8dd42ab6d-Paper.pdf>
- Ziyan Wang, Timur Bagautdinov, Stephen Lombardi, Tomas Simon, Jason Saragih, Jessica Hodgins, and Michael Zollhöfer. 2020. Learning Compositional Radiance Fields of Dynamic Human Heads. *arXiv:2012.09955* [cs.CV]
- Chung-Yi Weng, Brian Curless, Pratul P. Srinivasan, Jonathan T. Barron, and Ira Kemelmacher-Shlizerman. 2022. HumanNeRF: Free-viewpoint Rendering of Moving People from Monocular Video. *arXiv* (2022).
- Minye Wu, Yuehao Wang, Qiang Hu, and Jingyi Yu. 2020. Multi-View Neural Human Rendering. In *Proceedings of the IEEE/CVF Conference on Computer Vision and Pattern Recognition*. 1682–1691.
- Wenqi Xian, Jia-Bin Huang, Johannes Kopf, and Changil Kim. 2020. Space-time Neural Irradiance Fields for Free-Viewpoint Video. *arXiv:2011.12950* [cs.CV]
- Feng Xu, Yebin Liu, Carsten Stoll, James Tompkins, Gaurav Bharaj, Qionghai Dai, Hans-Peter Seidel, Jan Kautz, and Christian Theobalt. 2011. Video-based Characters: Creating New Human Performances from a Multi-view Video Database. In *ACM SIGGRAPH 2011 Papers (SIGGRAPH '11)*. ACM, New York, NY, USA, Article 32, 10 pages. <https://doi.org/10.1145/1964921.1964927>
- Hongyi Xu, Thiemo Alldieck, and Cristian Sminchisescu. 2021. H-NeRF: Neural Radiance Fields for Rendering and Temporal Reconstruction of Humans in Motion. *arXiv:2110.13746* [cs.CV]
- Lior Yariv, Jiatao Gu, Yoni Kasten, and Yaron Lipman. 2021. Volume rendering of neural implicit surfaces. In *Thirty-Fifth Conference on Neural Information Processing Systems*.
- Lior Yariv, Yoni Kasten, Dror Moran, Meirav Galun, Matan Atzmon, Basri Ronen, and Yaron Lipman. 2020. Multiview Neural Surface Reconstruction by Disentangling Geometry and Appearance. *Advances in Neural Information Processing Systems* 33 (2020).
- Alex Yu, Ruilong Li, Matthew Tancik, Hao Li, Ren Ng, and Angjoo Kanazawa. 2021. PlenOctrees for Real-time Rendering of Neural Radiance Fields. In *ICCV*.
- R. Zhang, P. Isola, A. A. Efros, E. Shechtman, and O. Wang. 2018. The Unreasonable Effectiveness of Deep Features as a Perceptual Metric. In *2018 IEEE/CVF Conference on Computer Vision and Pattern Recognition (CVPR)*. IEEE Computer Society, Los Alamitos, CA, USA, 586–595. <https://doi.org/10.1109/CVPR.2018.00068>
- Zhen Zhu, Tengting Huang, Baoguang Shi, Miao Yu, Bofei Wang, and Xiang Bai. 2019. Progressive Pose Attention Transfer for Person Image Generation. In *Proceedings of the IEEE Conference on Computer Vision and Pattern Recognition*. 2347–2356.
- C Lawrence Zitnick, Sing Bing Kang, Matthew Uyttendaele, Simon Winder, and Richard Szeliski. 2004. High-quality video view interpolation using a layered representation. In *ACM Transactions on Graphics (TOG)*, Vol. 23. ACM, 600–608.

A APPENDIX - OVERVIEW

In the following, we provide more implementation details (Section B), demonstrate applications, which our approach enables (Section C), and discuss some limitations (Section D).

B IMPLEMENTATION

In the following, we provide more details regarding the individual network architectures and training stages. As mentioned earlier, we pre-train f_{eg} and f_{Δ} as described in [Habermann et al. 2021].

Details for f_{tex} . For f_{tex} , we use the vid2vid [Wang et al. 2018] network with the default setting to predict texture maps at a resolution of 1024×1024 from normal maps in 1024×1024 . We trained vid2vid for about 30k iterations.

Details for f_{enc} and f_{nf} . For the texture encoder f_{enc} , we leverage the Tensorflow version of the pix2pix architecture [Isola et al. 2017]. We added two downsampling and two upsampling layers and adjusted the feature channel size in order to encode and decode images at a resolution of 1024×1024 . This network is trained jointly with f_{nf} . Important to note is that we train the encoder with the ground truth texture maps while we use the predicted texture maps only at test time. For f_{nf} , we leverage the architecture proposed by Mildenhall et al. [2020] with some changes. We changed the network depth to 16 for both the density prediction module as

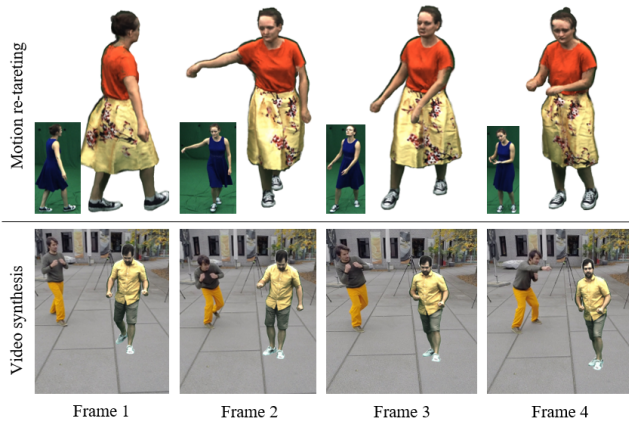


Fig. 10. Our method also enables exciting applications. Here, we show a motion re-targeting result of our method where we apply the motion of the actor with the blue dress on the actor with the yellow skirt. Moreover, our method can be used for video synthesis. To this end, we overlay our actors onto a dynamic video. For both applications, our method achieves photorealistic results.

well as the view-dependent branch. Further, we changed the number of activations of the density module and the view-dependent branch to 128 and 64, respectively. After every 4 fully connected layers we employ a skip connection. We train the network with the Adam optimizer [Kingma and Ba 2014] and employ a learning rate of 0.0005. Each training batch contains 1024 samples. We first train on downsampled images (1285×940) for 2 million iterations. Here, one batch contains 8 different camera views each sampling 128 rays for a randomly chosen frame. Then, the mesh is refined using the proposed NeRF-guided supervision, before f_{enc} and f_{inf} are once more trained for another 500k iterations using the refined geometry. Last, f_{enc} and f_{inf} are refined on the 4K images (4112×3008) for 1.5 million iterations. Here, we only sample 1 camera view and frame per batch.

Details for f_{δ} . For f_{δ} , we adopt the architecture proposed by Habermann et al. [2021]. We refine the pre-trained network for 360k iterations using the novel NeRF-guided loss. We weight the individual loss terms with $\lambda_{pc} = 5000.0$, $\lambda_{sil} = 50.0$, $\lambda_{laplacian} = 4000.0$, and $\lambda_{edge} = 0.075$.

C APPLICATIONS

In addition to view and motion synthesis, our method can also enable other exciting applications such as motion re-targeting. Figure 10 shows such an application setting where the actor with the blue dress is driving the actor with the yellow skirt. Note that the resulting images are very sharp and even small-scale wrinkles can be synthesized. Further, our method enables video synthesis where we augment an existing video with our virtual and photo-realistic characters.

D LIMITATIONS AND FUTURE WORK

Although our method achieves state-of-the-art results in terms of view and motion synthesis, it still has some limitations, which require future research in this direction. First, we currently do not capture and model hand gestures and facial expressions. This results sometimes in blurry results in these regions and these body parts can also not be explicitly controlled by the user. In the future, we plan to explore this direction to provide a fully controllable digital avatar. Moreover, our method does not model the incoming light independently from the reflectance properties of the surface. This comes with the limitation that the light is "baked-into" the appearance and novel lighting conditions cannot be synthesized. Here, a more explicit decomposition of light and material could potentially solve the problem. We rely on the motion tracking quality of our marker-less motion capture system and failures in the tracking can lead to artifacts in our results. To overcome this, one could jointly refine the skeletal pose by backpropagating the dense color losses through the entire neural rendering pipeline. Moreover, some artifacts around the boundary between the actor and the background arise from wrong ground truth segmentations during training. Here, we plan to investigate whether the pixel-wise classification can be jointly estimated during training. Last, even though our method is significantly more efficient than the baseline and capable of rendering 4K images within a few seconds, the training time could still be improved and the inference time is not yet real time. In the future, we would like to investigate alternative (potentially more lightweight) network designs [Chan et al. 2022; Fridovich-Keil and Yu et al. 2022; Garbin et al. 2021] and further explore the promising idea of hybrid representations.